

# Point-NeuS: Point-Guided Neural Implicit Surface Reconstruction by Volume Rendering

Chen Zhang, Wanjuan Su, Wenbing Tao\*

National Key Laboratory of Science and Technology on Multi-spectral Information Processing  
School of Artificial Intelligence and Automation, Huazhong University of Science and Technology, China  
{zhangchen\_, suwanjuan, wenbingtao}@hust.edu.cn

## Abstract

Recently, learning neural implicit surface by volume rendering has been a promising way for multi-view reconstruction. However, limited accuracy and excessive time complexity remain bottlenecks that current methods urgently need to overcome. To address these challenges, we propose a new method called Point-NeuS, utilizing point-guided mechanisms to achieve accurate and efficient reconstruction. Point modeling is organically embedded into the volume rendering to enhance and regularize the representation of implicit surface. Specifically, to achieve precise point guidance and noise robustness, aleatoric uncertainty of the point cloud is modeled to capture the distribution of noise and estimate the reliability of points. Additionally, a Neural Projection module connecting points and images is introduced to add geometric constraints to the Signed Distance Function (SDF). To better compensate for geometric bias between volume rendering and point modeling, high-fidelity points are filtered into an Implicit Displacement Network to improve the representation of SDF. Benefiting from our effective point guidance, lightweight networks are employed to achieve an impressive 11x speedup compared to NeuS. Extensive experiments show that our method yields high-quality surfaces, especially for fine-grained details and smooth regions. Moreover, it exhibits strong robustness to both noisy and sparse data.

## Introduction

Surface reconstruction from multiple calibrated views is a long-standing problem in computer vision and graphics. The traditional framework involves fusing depth maps from multi-view stereo (MVS) (Furukawa and Ponce 2009; Yao et al. 2018; Xu et al. 2022a; Wang et al. 2023) or depth cameras into a point cloud, followed by mesh extraction using point cloud surface reconstruction methods (Labatut, Pons, and Keriven 2007; Mostegel et al. 2017; Ma, Liu, and Han 2022). Although the traditional pipeline has proven techniques, it suffers from accumulating multi-stage errors and is restricted by the density and noise of the point cloud.

Recently, neural implicit surface reconstruction with volume rendering (Wang et al. 2021; Yariv et al. 2021) is highly valued for its potential to improve and simplify multi-view 3D reconstruction. These methods introduce the Signed Distance Function (SDF) to express opacity in the radiance

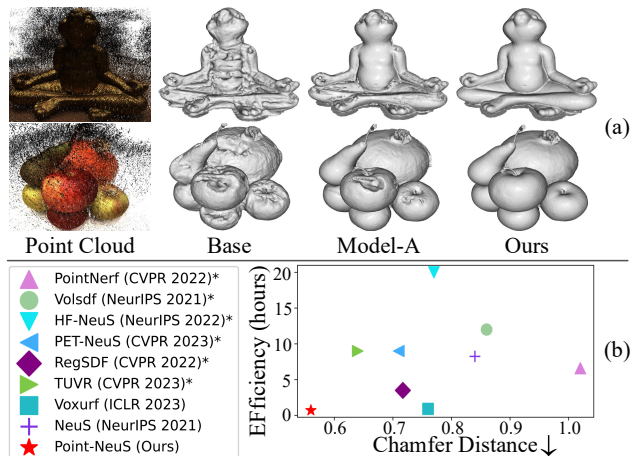


Figure 1: (a) Reconstruction results of our method with high-intensity noisy data. "Base" is the baseline for our method without point cloud inputs. "Model-A" is a naive point guidance mechanism as explained in our Preliminaries Section. (b) Comparison with SOTA methods on accuracy and efficiency. Our method achieves superior performance on both. \* indicates that the efficiency result is from technical paper.

field, enabling indirect SDF optimization during rendering. Impressively, photo-realistic color appearance and more complete geometry are modeled compared to the traditional framework. However, geometric bias in volume rendering (Fu et al. 2022; Zhang et al. 2023a) and excessive optimization time become its fly in the ointment.

To alleviate these problems, some methods introduce additional geometric priors to explicitly guide the implicit surface. For example, MonoSDF (Yu et al. 2022) uses depth and normal maps from monocular estimation to directly supervise the SDF network, while MVSDF (Zhang, Yao, and Quan 2021) works with depth information derived from an MVS network. Since these priors contain redundant geometric information, some methods opt for point clouds as a more reliable and concise alternative for supervisory signals. Dealing with point noise and maximizing the utility of reliable points becomes a crucial challenge for these methods. RegSDF (Zhang et al. 2022) designs a uniform smoothing term for all points to mitigate the impact of noisy data. However, such a manner fails to consider the variation of

\*Corresponding author.

noise with the region and also weakens the strong support provided by accurate point data. On the other hand, TUVr (Zhang et al. 2023a) takes confidence values output from the MVS network as an assessment of point reliability, assigning higher weights to points with greater confidence. Nevertheless, its reconstruction accuracy is still limited due to the unreliability of confidence maps as adjuncts to the MVS network. Additionally, these methods still need several hours or even longer for optimization, posing a challenge to achieving fast reconstruction. To fully exploit the potential of point clouds for high-quality guidance, several key challenges need to be addressed. 1) To mitigate the effects of noise, point reliability needs to be estimated simultaneously during surface optimization to achieve better results. 2) High-fidelity points should be fully utilized to achieve more accurate reconstruction. 3) With guaranteed accuracy, an efficient reconstruction scheme is urgently needed.

In this paper, we present Point-NeuS, a generic framework that organically combines point modeling and volume rendering to enhance and accelerate neural implicit surface reconstruction. Different from previous point-guided methods, we model the SDF value of each point as a Gaussian distribution. Aleatoric uncertainty estimation is introduced into point modeling to capture the distribution of inherent noise and estimate point reliability. Furthermore, we propose a Neural Projection module to constrain the SDF values of point data. Specifically, the points undergo two projections: first in space onto the implicit surface and then onto the image. Photometric consistency is computed to impose geometric constraints on the projected positions, effectively regularizing the SDF. Finally, a filter operation is performed with the modeled uncertainty, and high-fidelity points are fed into an Implicit Displacement Network to compensate for the geometric bias between volume rendering and point modeling. We conduct experiments on the DTU (Jensen et al. 2014) and BlendedMVS (Yao et al. 2020) datasets for evaluations. The results demonstrate the robustness of our approach across some challenging tasks, particularly with noisy point data (see Figure 1.a) and sparse point data. Moreover, benefiting from the outstanding point guidance, lightweight networks are allowed, enabling our approach to achieve an impressive 11x speedup compared to NeuS (Wang et al. 2021) without masks (see Figure 1.b). In summary, our contributions are as follows:

- Point modeling and volume rendering are organically integrated to guide accurate and efficient surface reconstruction.
- By employing uncertainty modeling to capture inherent noise and a Neural Projection module to regularize the SDF, strong robustness against point noise is exhibited.
- The Implicit Displacement Function compensates for the geometric bias between volume rendering and point modeling, leading to more precise implicit surfaces.

## Related Work

**Traditional multi-view reconstruction.** Traditional multi-view reconstruction typically involves two steps: fusing depth maps obtained from MVS (Zhang et al. 2023b; Su and

Tao 2023; Ding et al. 2022) or depth cameras into a point cloud, followed by employing point cloud surface reconstruction algorithms (Sitzmann et al. 2020; Ma et al. 2021) to generate a mesh. Classical screened Poisson Surface Reconstruction (sPSR) (Kazhdan and Hoppe 2013) is a widely used technique to generate watertight surfaces from point clouds. Although the traditional pipeline has made successive breakthroughs in reconstruction quality due to accumulated technical progress, there are still challenges of sensitivity to point cloud noise and density.

**Multi-view neural implicit surface reconstruction.** Recently, with the development of differentiable rendering (Aliev et al. 2020; Bangaru et al. 2022), neural implicit surface reconstruction (Yariv et al. 2020; Yang et al. 2022) is valued for its single-stage optimization and strong representation potential. Nerf (Mildenhall et al. 2021) is a pioneer in combining volume rendering and neural implicit representation for high-quality rendering, triggering plenty of works (Martin-Brualla et al. 2021; Xu et al. 2022b; Pan et al. 2022) to represent scenes in this framework. To improve geometric quality, VolSDF (Yariv et al. 2021) and NeuS (Wang et al. 2021) design new weight functions involving SDF for color accumulation in the rendering. Compared to traditional pipelines, these methods not only render photo-realistic appearances but also reconstruct more complete surfaces, especially for non-Lambertian surfaces. However, geometric bias is still an urgent problem due to discrete sampling and other factors (Fu et al. 2022; Zhang et al. 2023a). Additionally, the scarcity of details and lengthy optimization also hinder their broader application. Subsequent methods (Wang, Skorokhodov, and Wonka 2022, 2023) try to solve these problems, but still struggle to strike an accuracy-efficiency balance. Impressively, some methods use voxel-based representation to enhance training efficiency, such as Voxurf (Wu et al. 2023) and Vox-Surf (Li et al. 2022), making significant strides in achieving this equilibrium. Both employ complex CUDA acceleration techniques, while our method achieves comparable speed without relying on these.

**Geometry supervision for neural implicit reconstruction.** To achieve high-quality reconstruction, some methods (Jiang et al. 2023; Zhu et al. 2023) introduce additional geometric information to explicitly guide the geometry modeling. MonoSDF (Yu et al. 2022) employs monocular normal and depth cues to supervise the SDF network. MVSDF (Zhang, Yao, and Quan 2021) introduces depth maps and depth feature maps from an MVS network to aid geometric representation. Related to our method, RegSDF (Zhang et al. 2022) and TUVr (Zhang et al. 2023a) use point clouds as supervisory signals, enhancing scene representation while accounting for point noise. RegSDF smooths all data by constraining the second derivative, which overlooks noise variation across regions. On the other hand, TUVr simply relies on confidence value output by the MVS network to avoid this problem. In contrast, our method introduces uncertainty to capture the distribution of noise, allowing surface optimization and point reliability assessment to be mutually reinforcing. Moreover, although the additional geometry pri-

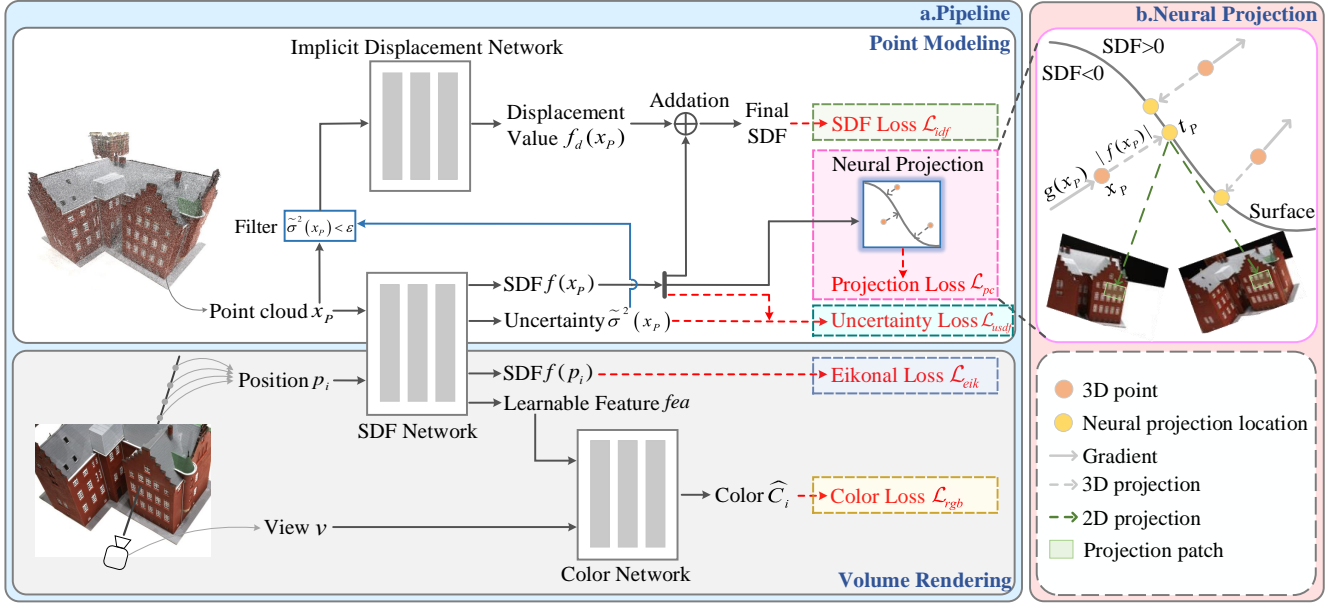


Figure 2: The overview of Point-NeuS. Our network integrates point modeling with volume rendering through the SDF network, enhancing scene representation. NeuS serves as the base framework for the volume rendering part, while the point modeling part focuses on improving the quality of surface guidance. To this end, uncertainty estimation and the Neural Projection module are designed to attenuate the effect of noise, allowing accurate reconstruction. Additionally, the Implicit Displacement Network further learns to compensate for the geometric bias between volume rendering and point modeling for high-fidelity data.

ors accelerate the convergence of these methods, they still require several hours to optimize a scene. Thus, an efficient implementation is still desperately needed.

## Preliminaries

**Reconstruction from volume rendering.** NeuS (Wang et al. 2021) is a very popular method for neural implicit surface reconstruction. It represents the surface as the zero-level set of SDF  $\mathcal{S} = \{x \in \mathbb{R}^3 | f(x) = 0\}$ . In rendering, a ray emitting from the camera center  $o$  along the direction  $d$  that passes through a pixel can be expressed as  $\{p(t) = o + td | t > 0\}$ . The rendered color  $\hat{C}$  of this pixel is accumulated along the ray with  $N$  discrete sampled points.

$$\hat{C} = \sum_{i=1}^N T_i \alpha_i c_i, \quad T_i = \prod_{j=1}^{i-1} (1 - \alpha_j) \quad (1)$$

where  $\alpha_i$  is the discrete opacity, and  $T_i$  is the accumulated transmittance. To reduce the estimation bias of SDF, NeuS defines the opacity as follows:

$$\alpha_i = \max\left(\frac{\Phi_s(f(p(t_i))) - \Phi_s(f(p(t_{i+1})))}{\Phi_s(f(p(t_i)))}, 0\right) \quad (2)$$

Here,  $\Phi_s(x) = (1 + e^{-sx})^{-1}$  is the Sigmoid function, where the  $s$  value is a trainable parameter.

**Naive point guidance.** Given a point cloud  $\{P | x_P \in P\}$ , a straightforward guidance for neural implicit surface reconstruction is to assume that all points are distributed over the implicit surface, such that the SDF network can be effectively supervised by  $\{f(x_P) = 0\}$ . However, in reality, the

point cloud distribution varies around the implicit surface, leading to varying degrees of noise across different regions. The key to achieving high-quality reconstruction lies in effectively removing noise and leveraging high-fidelity points to enhance detail expression.

## Method

Given a set of RGB images with known camera parameters, our aim is to accurately reconstruct geometry within the volume rendering framework. To counteract the inherent geometric bias in the rendering, a point cloud is additionally introduced as the guidance for the implicit surface to achieve high-quality and efficient reconstruction. The pipeline of our method is illustrated in Figure 2.a.

### Point Cloud Generation

Point clouds can be obtained by fusing depth maps obtained from MVS or depth cameras. For simplicity, we use TransMVSNet (Ding et al. 2022) with robust generalization ability to generate a depth map for each view. Proper geometric consistency filtering is performed in the fusion process to produce relatively accurate and clean point clouds. Principle component analysis is used to estimate the normals and their directions are corrected according to the camera positions.

### Uncertainty Estimation

In Bayesian deep learning (Kendall and Gal 2017; Lakshminarayanan, Pritzel, and Blundell 2017), the inherent noise of the observed data is modeled as aleatoric uncertainty. Inspired by this, we learn the uncertainty for the input point cloud to capture the distribution of noise. For each 3D point

$x_P$  in  $P$ , its SDF value is modeled as a Gaussian distribution rather than a single value, where the predicted variance can reflect the aleatoric uncertainty of  $x_P$ . Considering that the noise varies across regions, each point is allowed to learn a different variance. As a result, the model provides a large variance for points with high noise, rather than collapsing to a trivial solution. The learning of heteroscedastic aleatoric uncertainty can well help our method capture complex noise for better geometry optimization.

Specifically, the SDF value of a point  $x_P$  in  $P$  is output as a Gaussian distribution parameterized by mean  $f(x_P)$  and variance  $\tilde{\sigma}^2(x_P)$ . We take the output of the SDF network as the mean and add an additional header to model the variance.

$$f(x_P), \sigma^2(x_P), fea = MLP_{sdf}(x_P) \quad (3)$$

$fea$  is the feature vector fed into the color network, but we do not use it for point modeling. Softplus function is further adopted to  $\sigma^2$  to produce a valid variance value. Then a minimum variance constraint  $\sigma_0^2$  is added for all points.

$$\tilde{\sigma}^2(x_P) = \sigma_0^2 + \log(1 + \exp(\sigma^2(x_P))) \quad (4)$$

To optimize the model, we assume that the SDF values of all points fluctuate around the 0 value. This assumption is reasonable since the ideal point cloud is distributed over a 0-value surface. Therefore, following the theoretical guidance of Bayesian deep learning (Kendall and Gal 2017), the negative log-likelihood of a point set is optimized in the regression as follows:

$$\begin{aligned} \mathcal{L}_{usdf} &= -\frac{1}{D_P} \sum_{x_P \in P} \log p_\theta(f_\varepsilon(x_P)) \\ &= \frac{1}{D_P} \sum_{x_P \in P} \frac{\|f_\varepsilon(x_P) - f(x_P)\|_2^2}{2\tilde{\sigma}^2(x_P)} + \frac{\log \tilde{\sigma}^2(x_P)}{2} \end{aligned} \quad (5)$$

where  $D_P$  represents the number of points in the set  $P$ , and  $f_\varepsilon(x_P)$  denotes the ideal SDF value for  $x_P$ , which is set to 0. In the first term in the loss, large value of  $\tilde{\sigma}^2(x_P)$  reduces the importance assigned to a point with high noise, thereby mitigating adverse effects. The second term is a regularization term to avoid predicting infinite variance for all points.

### Neural Projection Module

In order to enhance the prediction accuracy of SDF values for points while further enforcing geometric constraints on noisy data, a Neural Projection module is designed to regularize the SDF field using photometric consistency. As shown in Figure 2.b, for a point  $x_P$ , we use the predicted SDF value  $f(x_P)$  and the gradient  $g(x_P)$  to project it to the nearest neighbor  $t_P$  on the implicit surface  $\mathcal{S}$ . The gradient  $g(x_P)$  represents the direction vector with the fastest increasing SDF value at  $x_P$ , which is also denoted as  $\nabla f(x_P)$ . Therefore,  $t_P$  can be obtained by moving  $x_P$  along or against the direction of  $g(x_P)$  by a distance of  $|f(x_P)|$ .

$$t_P = x_P - f(x_P) \times \nabla f(x_P) / \|\nabla f(x_P)\|_2 \quad (6)$$

The direction of  $g(x_P)$  is always toward the outside of surface  $\mathcal{S}$ . Therefore, Equation 6 can determine whether to

move  $x_P$  along or against the direction of  $g(x_P)$  depending on the positive or negative value of  $f(x_P)$ .

In fact, the accuracy of learned projection distance is consistent with the accuracy of constructed implicit surface. To ensure that  $t_P$  is distributed on the real surface, we use the photometric consistency constraint from MVS to supervise the position of  $t_P$ . For a small area  $s$  on the surface where  $t_P$  is located, its projection patches in different views are supposed to be geometry-consistent. The photometric consistency is determined by calculating the normalization cross-correlation (NCC) of patches between the reference image  $I_r$  and the source image  $I_s$  according to Equation 7. The image corresponding to the depth map that generates  $x_P$  is taken as the reference image and the rest as source images. Referring to Geo-Neus (Fu et al. 2022), we use gray images for computing NCC scores to focus more on geometric information, and select the best four ones among all source images to calculate the photometric consistency loss  $\mathcal{L}_{pc}$ .

$$NCC(I_r(s), I_s(s)) = \frac{Cov(I_r(s), I_s(s))}{\sqrt{Var(I_r(s))Var(I_s(s))}} \quad (7)$$

where  $Cov$  is covariance and  $Var$  is variance.  $I_r(s)$  and  $I_s(s)$  are the patches of  $s$  projecting to  $I_r$  and  $I_s$ , respectively.  $\mathcal{L}_{pc}$  is calculated as follows:

$$\mathcal{L}_{pc} = \frac{1}{4D_P} \sum_{x_P \in P} \sum_{i=1}^4 (1 - NCC(I_r(s), I_{si}(s))) \quad (8)$$

where  $D_P$  is the number of points in the set  $P$ . The photometric consistency loss imposes a strong geometric constraint on the projection position  $t_P$ , indirectly ensuring the accuracy of the predicted SDF value at  $x_P$ . This point-to-image constraint benefits better SDF representations.

### Implicit Displacement Network

To achieve superior point guidance, it is not only essential to eliminate noise-related effects, but also to utilize high-fidelity data for more precise reconstruction. For each point  $x_P$  with a predicted variance  $\tilde{\sigma}^2(x_P)$ , a larger  $\tilde{\sigma}^2(x_P)$  represents a higher uncertainty for  $x_P$ . To focus on the reliable points with low uncertainty, we perform a filtering operation to extract the point set  $P_s$  with a variance below the threshold  $\varepsilon$ , i.e.,  $\{P_s | x_P \in P_s, \tilde{\sigma}^2(x_P) < \varepsilon\}$ .  $P_s$  is further fed to an Implicit Displacement Network to capture the geometric bias between volume rendering and point modeling. It is worth noting that this Implicit Displacement Network specifically designed for high-fidelity points works independently of the volume rendering. With the SDF network in volume rendering taken as the base SDF network, the final SDF value of  $x_P$  is the sum of the Implicit Displacement Function (IDF) value  $f_d(x_P)$  and the base SDF value  $f(x_P)$ . The whole process is formulated as follows:

$$f_d(x_P) = MLP_{idf}(x_P) \quad (9)$$

$$f_{final}(x_P) = f(x_P) + f_d(x_P) \quad (10)$$

Furthermore, we design a SDF loss to optimize the model.

$$\mathcal{L}_{idf} = \frac{1}{D_{P_s}} \sum_{x_P \in P_s} |f_\varepsilon(x_P) - f_{final}(x_P)| \quad (11)$$

Scan ID	24	37	40	55	63	65	69	83	97	105	106	110	114	118	122	Mean
sPSR <sub>0</sub>	0.49	1.27	0.63	0.57	0.88	0.69	0.53	1.37	0.93	0.76	0.60	0.86	0.30	0.51	0.70	0.74
sPSR <sub>7</sub>	0.47	1.10	0.44	0.34	0.81	0.69	0.53	1.21	0.91	0.68	0.51	0.70	0.30	0.40	0.48	0.64
SIREN	0.56	1.05	0.46	0.44	1.15	0.88	1.56	1.95	1.87	0.78	1.22	1.16	1.78	1.50	0.53	1.13
VolSDF	1.14	1.26	0.81	0.49	1.25	0.70	0.72	1.29	1.18	0.70	0.66	1.08	0.42	0.61	0.55	0.86
NeuS	1.00	1.37	0.93	0.43	1.10	0.65	0.57	1.48	1.09	0.83	0.52	1.20	0.35	0.49	0.54	0.84
Instant-NeuS	0.59	0.91	0.97	0.35	1.21	0.64	0.84	1.31	1.44	0.79	0.62	1.09	0.53	0.80	0.50	0.84
NeuralWarp	0.49	0.71	0.38	0.38	0.79	0.81	0.82	1.20	1.06	0.68	0.66	0.74	0.41	0.63	0.51	0.68
HF-NeuS	0.76	1.32	0.70	0.39	1.06	0.63	0.63	1.15	1.12	0.80	0.52	1.22	0.33	0.49	0.50	0.77
Voxurf	0.72	0.75	0.47	0.39	1.47	0.76	0.81	1.02	1.04	0.92	0.52	1.13	0.40	0.53	0.53	0.76
PET-NeuS	0.56	0.75	0.68	0.36	0.87	0.76	0.69	1.33	1.08	<b>0.66</b>	0.51	1.04	0.34	0.51	0.48	0.71
NeuDA	0.47	<b>0.71</b>	0.42	0.36	0.88	0.56	0.56	1.43	1.04	0.81	0.51	0.78	0.32	0.41	0.45	0.65
COLMAP	0.81	2.05	0.73	1.22	1.79	1.58	1.02	3.05	1.40	2.05	1.00	1.32	0.49	0.78	1.17	1.36
MVSDF	0.83	1.76	0.88	0.44	1.11	0.90	0.75	1.26	1.02	1.35	0.87	0.84	0.34	0.47	0.46	0.88
PointNeRF	0.87	2.06	1.20	1.01	1.01	1.39	0.80	1.04	0.92	0.74	0.97	0.76	0.56	0.90	1.05	1.02
MonoSDF	0.66	0.88	0.43	0.40	0.87	0.78	0.81	1.23	1.18	<b>0.66</b>	0.66	0.96	0.41	0.57	0.51	0.73
RegSDF	0.597	1.410	0.637	0.428	1.342	0.623	0.599	<b>0.895</b>	0.919	1.020	0.600	<b>0.594</b>	<b>0.297</b>	0.406	0.389	0.717
TUVR	0.56	0.92	0.39	0.39	0.85	0.58	0.51	1.20	0.90	0.78	0.42	0.84	0.32	0.43	0.44	0.64
Ours	<b>0.338</b>	0.822	<b>0.403</b>	<b>0.331</b>	<b>0.754</b>	<b>0.541</b>	<b>0.493</b>	1.128	<b>0.855</b>	0.713	<b>0.367</b>	0.606	0.302	<b>0.371</b>	<b>0.378</b>	<b>0.560</b>

Table 1: Quantitative comparison results with different state-of-the-art (SOTA) methods on DTU without masks.

where  $D_{P_s}$  is the number of points in  $P_s$ , and  $f_\varepsilon(x_P)$  is the ideal SDF value of  $x_P$ , which is set to 0. With the loss, the network learns a more accurate representation of the regions where high-fidelity points are located. For more details about the network, please refer to the supplementary.

### Loss Function

Similar to previous works, we use L1 loss to minimize the difference between the ground truth colors and the rendered colors:

$$\mathcal{L}_{rgb} = \frac{1}{N} \sum_{i=1}^N |C_i - \hat{C}_i| \quad (12)$$

where  $N$  is the number of a batch rays. Eikonal loss is also added to regularize the SDF field.

$$\mathcal{L}_{eik} = \frac{1}{MN} \sum_{i,j=1}^{MN} \|\nabla f(p_{i,j}) - 1\|^2 \quad (13)$$

where  $M$  is the number of sampled locations on each ray.

In order to speed up the convergence of the SDF network, we additionally add normal constraints from the point cloud. We calculate  $\mathcal{L}_1$  loss and cosine loss for the normals as follows:

$$\mathcal{L}_1 = \frac{1}{D_P} \sum_{x_P \in P} |\nabla f(x_P) - n_{x_P}| \quad (14)$$

$$\mathcal{L}_{cos} = \frac{1}{D_P} \sum_{x_P \in P} |1 - \nabla f(x_P) \odot n_{x_P}| \quad (15)$$

where  $D_P$  is the number of points in point set  $P$ .  $n_{x_P}$  is the unit normal vector of point  $x_P$ .  $\odot$  is a dot product operation. There is the final normal loss  $\mathcal{L}_n = \mathcal{L}_1 + \mathcal{L}_{cos}$ . Then the total loss is defined as:

$$\mathcal{L} = \mathcal{L}_{rgb} + \lambda_1 \mathcal{L}_{eik} + \lambda_2 \mathcal{L}_{usdf} + \lambda_3 \mathcal{L}_{idf} + \lambda_4 \mathcal{L}_{pc} + \lambda_5 \mathcal{L}_n \quad (16)$$

In our experiments, we choose  $\lambda_1 = 0.1$ ,  $\lambda_2 = 1$ ,  $\lambda_3 = 1$ ,  $\lambda_4 = 0.25$ ,  $\lambda_5 = 0.1$ . To avoid introducing errors about the normals, we change  $\lambda_5$  to 0.01 after some iterations.

	NeuS	Voxurf	Ours
Time (RTX 3090)	8.25 hours	55mins	<b>43mins</b>
GPU Memory	6.84GB	23.55GB	<b>4.88GB</b>

Table 2: Comparison of our method with Voxurf and NeuS in terms of efficiency and GPU memory usage.

## Experiments

### Experimental Setting

**Datasets.** Following previous works, we use 15 scenes from the DTU dataset (Jensen et al. 2014) for quantitative and qualitative evaluations, which include challenging cases, such as low-texture areas, thin structures, and specular reflection. Chamfer Distance (CD) is taken as the evaluation metric. Additionally, we also select several challenging scenes from the low-res BlendedMVS dataset (Yao et al. 2020) for qualitative comparisons.

**Network architecture.** Our network is built based on NeuS with light MLPs. The base SDF network is parameterized by a 4-layer MLP with 256 hidden units and the Implicit Displacement Network is parameterized by a similar 2-layer MLP. We also use a 2-layer MLP with 128 hidden units to construct the color network. To enhance learning efficiency, the popular InstantNGP (Müller et al. 2022) is utilized to encode the input position information of the three networks using the same parameters as MonoSDF (Yu et al. 2022).

**Implementation details.** We use pre-trained TransMVSNet (Ding et al. 2022) on DTU to provide reliable depth map and point cloud for each view. To ensure fairness, we exclude the tested scenes from its original training set and retrain it on DTU. The time for depth prediction is about one second per image, thus the total preprocessing time is relatively short. The final point cloud contains about tens of millions of points. To demonstrate that our method does not rely on overly dense data, we downsample it to 2 million points by interval, i.e., sampling one point every  $k$  points. This manner works well to balance efficiency while preserving the distri-



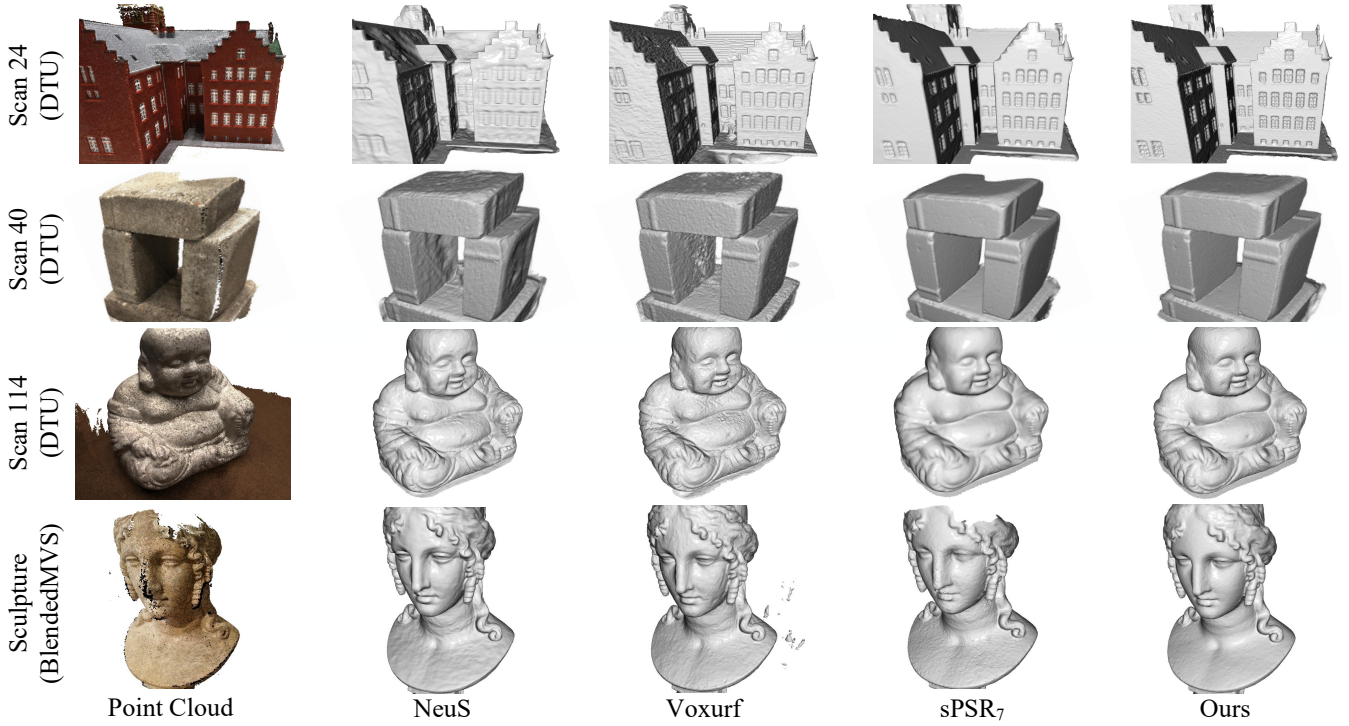


Figure 3: Qualitative comparison of our approach with methods from different categories on DTU and BlendedMVS.

bution characteristics of raw data. Furthermore, to facilitate the image projection in our Neural Projection module, we pick the point set generated by the current view to feed into the network at each iteration. In each batch, 512 rays and 1024 points are randomly sampled. We experiment on a single RTX 3090 GPU, optimizing for  $30k$  steps for around 43 minutes on each scene with a batch size of 1. Please refer to the supplementary material for more details.

**Baselines.** We compare our method with **1)** sPSR (Kazhdan and Hoppe 2013), which is a classic geometric surface reconstruction method from point cloud. **2)** SIREN (Sitzmann et al. 2020), which is a popular learning-based implicit reconstruction method from point cloud. **3)** VolSDF (Yariv et al. 2021), NeuS (Wang et al. 2021), NeuralWarp (Darmon et al. 2022), HF-NeuS (Wang, Skorokhodov, and Wonka 2022), Voxurf (Wu et al. 2023), PET-NeuS (Wang, Skorokhodov, and Wonka 2023) and NeuDA (Cai et al. 2023), which are neural implicit surface reconstruction methods with volume rendering. We also compare Instant-NeuS, which is a NeuS implementation using InstantNGP (Müller et al. 2022), referring to NeuDA for details. **4)** MVSDf (Zhang, Yao, and Quan 2021), PointNeRF (Xu et al. 2022b), MonoSDF (Yu et al. 2022), RegSDF (Zhang et al. 2022) and TUVr (Zhang et al. 2023a), which use geometric priors to supervise neural implicit reconstruction. In addition, COLMAP (Schönberger et al. 2016) is also added.

## Comparisons

As shown in Table 1, we report the quantitative comparison results of our method with different methods on the DTU dataset without masks. The results of all compared neural implicit methods are derived from their original papers. Spe-

cially, the results of Instant-NeuS and COLMAP are from the NeuDA paper (Cai et al. 2023), and the result of PointNeRF is from the Voxurf paper (Wu et al. 2023). For sPSR, we report two results with trimming values set to 0 and 7. Although sPSR<sub>7</sub> scores higher than sPSR<sub>0</sub>, the surface integrity is compromised. In addition, the mask cropping provided by NeuS is also applied to the results of sPSR and SIREN for fair comparisons. Importantly, both methods utilize unsampled input point clouds as input, making the comparison more challenging. In the comparison with diverse baselines, our method shows significant advantages with a 12.5% improvement over the SOTA method.

Moreover, benefiting from effective point guidance and lightweight networks, our approach strikes a good balance between efficiency and accuracy. In contrast to other methods that require several hours or even more than ten hours for optimization, our method and Voxurf complete the task within one hour. Table 2 further shows a detailed comparison of our approach with Voxurf (Wu et al. 2023) and NeuS (Wang et al. 2021) in terms of efficiency and resource usage. Compared to Voxurf using multiple CUDA acceleration techniques for networks and sampling, our method achieves superior speed without relying on these, except for Instant-NGP’s CUDA implementation. The 11x speedup compared to NeuS and the 21.8% speedup compared to Voxurf demonstrate the high efficiency of our method. As another advantage, it possesses a low GPU memory usage.

Figure 3 presents a qualitative comparison of our method with other methods. Our approach combines the advantages brought by volume rendering and point modeling, resulting in improved reconstruction outcomes. Compared to other neural implicit surface reconstruction methods, richer fine-

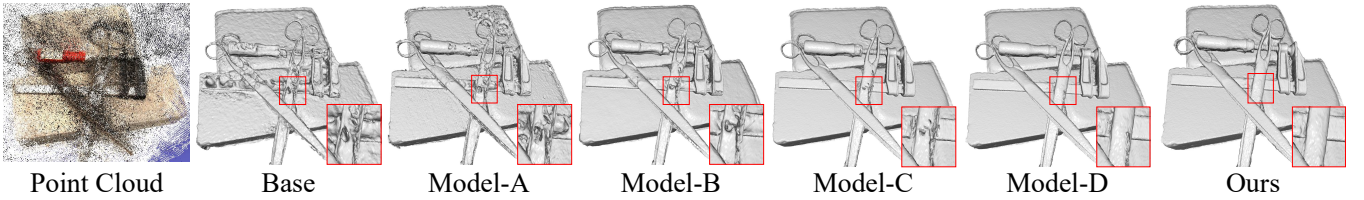


Figure 4: Visual results of different baselines when point clouds without geometric consistency filtering are taken as input.

Method	$\mathcal{L}_{sdf}$	$\mathcal{L}_{pc}$	$\mathcal{L}_{usdf}$	$\mathcal{L}_{idf}$	CD
Base					1.059
Model-A	✓				0.687
Model-B	✓	✓			0.649
Model-C			✓		0.582
Model-D		✓	✓		0.569
Ours		✓	✓	✓	<b>0.560</b>

Table 3: Ablation study on DTU.

grained details are characterized by our method, such as windows in Scan24. Moreover, smoother surfaces are also reconstructed, like flat areas in Scan40 and curved ones in Scan114. Compared to sPSR, more complete surfaces and better noise robustness are presented by our method, such as the nose in Sculpture.

## Analysis

**Ablation study.** In order to evaluate the improvement brought by point guidance compared to the base framework and the effect of each module in our method, we conduct an ablation study on the DTU dataset, as presented in Table 3. First, by removing the point modeling part of our pipeline, we only keep the volume rendering part as the Base model. Subsequently, we introduce the point cloud and a simple loss  $\mathcal{L}_{sdf}$  as Model-A, which is equivalent to  $\mathcal{L}_{usdf}$  with  $\tilde{\sigma}^2(x_P)$  treated as a constant value in uncertainty estimation, to compare the effects brought by a naive point guidance. On this basis, the Neural Projection module is added as Model-B, and replacing  $\mathcal{L}_{sdf}$  with  $\mathcal{L}_{usdf}$  is taken as Model-C, to evaluate the individual effects of the two modules. The combination of the two modules is referred to as Model-D. Finally, the Implicit Displacement Network is added as our current model. Except for the Base model, all other models apply the point normal loss to ensure a fair comparison. It is evident that each module in our method contributes to higher-precision reconstruction, demonstrating the effectiveness of each module. More meaningfully, the significant improvement achieved by our approach, serving as a generic framework built on lightweight NeuS, demonstrates the strong potential of the point guidance mechanism.

**Noise resistance.** To test the robustness of our method to noisy point clouds, we perform experiments on two types of noisy data. The first type is a high-intensity noisy point cloud without any geometric consistency filtering during depth maps fusion, and the reconstruction results are presented in Figure 4. Additionally, the results of each baseline in Table 3 are also presented, further demonstrating the resistance of each module to high-intensity noisy data. To more clearly quantify noise intensity, we apply artificial noise to

Proportion	0%	10%	15%	20%	25%	30%
CD	<b>0.560</b>	0.565	0.571	0.576	0.588	0.602

Table 4: Quantitative results of applying Gaussian noise to points of different proportions.

Number	5M	2M	1M	0.5M	0.1M
CD	<b>0.560</b>	<b>0.560</b>	0.565	0.572	0.575

Table 5: Quantitative results with different number of points.

the point cloud as the second type of noisy data. We randomly select different percentages of points from the point cloud to add high-intensity Gaussian noise with a standard deviation of 50%. As shown in Table 4, as the noise intensity increases significantly, our CD value still maintains a small fluctuation, demonstrating strong robustness to noise.

**Adaptation to density variations.** Adaptability to sparse data is also an important challenge for point-guided methods, reflecting the robustness to complex extreme cases. As shown in Table 5, we downsample the raw points to different numbers to test the adaptability of our method for sparse data. It can be seen that our method remains a robust performance even as the point density significantly decreases. Satisfyingly, for very sparse one hundred thousand points, we still maintain an excellent result.

**Limitations.** Reconstruction of non-visible regions remains a bottleneck in our approach. In these regions, point data is usually not generated, making it difficult to achieve effective surface guidance. This is also a common problem faced by current multi-view reconstruction. It would be a good direction to combine other generative models in future work.

## Conclusion

We propose Point-NeuS, a novel point-guided method for multi-view neural surface reconstruction, giving an effective solution to resist geometric ambiguity in rendering and achieving accurate and efficient reconstruction. Uncertainty estimation and the Neural Projection module lead to high-quality point guidance and enhance the robustness of our method against point noise. Furthermore, the Implicit Displacement Network allows our method to learn a more precise geometric representation. Experiments demonstrate the superiority of our method in reconstruction accuracy and efficiency, as well as the robustness against some challenging data, such as high-intensity noisy data and sparse data. We expect that the potential of combining volume rendering and point cloud reconstruction is further explored by more methods, contributing to high-quality reconstruction.

## References

- Aliiev, K.-A.; Sevastopolsky, A.; Kolos, M.; Ulyanov, D.; and Lempitsky, V. 2020. Neural point-based graphics. In *Computer Vision—ECCV 2020: 16th European Conference, Glasgow, UK, August 23–28, 2020, Proceedings, Part XXII 16*, 696–712. Springer.
- Bangaru, S. P.; Gharbi, M.; Luan, F.; Li, T.-M.; Sunkavalli, K.; Hasan, M.; Bi, S.; Xu, Z.; Bernstein, G.; and Durand, F. 2022. Differentiable rendering of neural sdfs through reparameterization. In *SIGGRAPH Asia 2022 Conference Papers*, 1–9.
- Cai, B.; Huang, J.; Jia, R.; Lv, C.; and Fu, H. 2023. NeuDA: Neural Deformable Anchor for High-Fidelity Implicit Surface Reconstruction. In *Proceedings of the IEEE/CVF Conference on Computer Vision and Pattern Recognition*, 8476–8485.
- Darmon, F.; Bascle, B.; Devaux, J.-C.; Monasse, P.; and Aubry, M. 2022. Improving neural implicit surfaces geometry with patch warping. In *Proceedings of the IEEE/CVF Conference on Computer Vision and Pattern Recognition*, 6260–6269.
- Ding, Y.; Yuan, W.; Zhu, Q.; Zhang, H.; Liu, X.; Wang, Y.; and Liu, X. 2022. Transmvsnet: Global context-aware multi-view stereo network with transformers. In *Proceedings of the IEEE/CVF Conference on Computer Vision and Pattern Recognition*, 8585–8594.
- Fu, Q.; Xu, Q.; Ong, Y. S.; and Tao, W. 2022. Geo-neus: Geometry-consistent neural implicit surfaces learning for multi-view reconstruction. *Advances in Neural Information Processing Systems*, 35: 3403–3416.
- Furukawa, Y.; and Ponce, J. 2009. Accurate, dense, and robust multiview stereopsis. *IEEE transactions on pattern analysis and machine intelligence*, 32(8): 1362–1376.
- Jensen, R.; Dahl, A.; Vogiatzis, G.; Tola, E.; and Aanaes, H. 2014. Large scale multi-view stereopsis evaluation. In *Proceedings of the IEEE conference on computer vision and pattern recognition*, 406–413.
- Jiang, H.; Zeng, C.; Chen, R.; Liang, S.; Han, Y.; Gao, Y.; and Wang, C. 2023. Depth-NeuS: Neural Implicit Surfaces Learning for Multi-view Reconstruction Based on Depth Information Optimization. *arXiv preprint arXiv:2303.17088*.
- Kazhdan, M.; and Hoppe, H. 2013. Screened poisson surface reconstruction. *ACM Transactions on Graphics (ToG)*, 32(3): 1–13.
- Kendall, A.; and Gal, Y. 2017. What uncertainties do we need in bayesian deep learning for computer vision? *Advances in neural information processing systems*, 30.
- Labatut, P.; Pons, J.-P.; and Keriven, R. 2007. Efficient multi-view reconstruction of large-scale scenes using interest points, delaunay triangulation and graph cuts. In *2007 IEEE 11th international conference on computer vision*, 1–8. IEEE.
- Lakshminarayanan, B.; Pritzel, A.; and Blundell, C. 2017. Simple and scalable predictive uncertainty estimation using deep ensembles. *Advances in neural information processing systems*, 30.
- Li, H.; Yang, X.; Zhai, H.; Liu, Y.; Bao, H.; and Zhang, G. 2022. Vox-surf: Voxel-based implicit surface representation. *IEEE Transactions on Visualization and Computer Graphics*.
- Ma, B.; Han, Z.; Liu, Y.-S.; and Zwicker, M. 2021. Neural-Pull: Learning Signed Distance Functions from Point Clouds by Learning to Pull Space onto Surfaces. In *Proceedings of the 38th International Conference on Machine Learning*, volume 139.
- Ma, B.; Liu, Y.-S.; and Han, Z. 2022. Reconstructing surfaces for sparse point clouds with on-surface priors. In *Proceedings of the IEEE/CVF Conference on Computer Vision and Pattern Recognition*, 6315–6325.
- Martin-Brualla, R.; Radwan, N.; Sajjadi, M. S.; Barron, J. T.; Dosovitskiy, A.; and Duckworth, D. 2021. Nerf in the wild: Neural radiance fields for unconstrained photo collections. In *Proceedings of the IEEE/CVF Conference on Computer Vision and Pattern Recognition*, 7210–7219.
- Mildenhall, B.; Srinivasan, P. P.; Tancik, M.; Barron, J. T.; Ramamoorthi, R.; and Ng, R. 2021. Nerf: Representing scenes as neural radiance fields for view synthesis. *Communications of the ACM*, 65(1): 99–106.
- Mostegel, C.; Prettenhaler, R.; Fraundorfer, F.; and Bischof, H. 2017. Scalable surface reconstruction from point clouds with extreme scale and density diversity. In *Proceedings of the IEEE Conference on Computer Vision and Pattern Recognition*, 904–913.
- Müller, T.; Evans, A.; Schied, C.; and Keller, A. 2022. Instant neural graphics primitives with a multiresolution hash encoding. *ACM Transactions on Graphics (ToG)*, 41(4): 1–15.
- Pan, X.; Lai, Z.; Song, S.; and Huang, G. 2022. Activenet: Learning where to see with uncertainty estimation. In *European Conference on Computer Vision*, 230–246. Springer.
- Schönberger, J. L.; Zheng, E.; Frahm, J.-M.; and Pollefeys, M. 2016. Pixelwise view selection for unstructured multi-view stereo. In *Computer Vision—ECCV 2016: 14th European Conference, Amsterdam, The Netherlands, October 11–14, 2016, Proceedings, Part III 14*, 501–518. Springer.
- Sitzmann, V.; Martel, J.; Bergman, A.; Lindell, D.; and Wetzstein, G. 2020. Implicit neural representations with periodic activation functions. *Advances in neural information processing systems*, 33: 7462–7473.
- Su, W.; and Tao, W. 2023. Efficient Edge-Preserving Multi-View Stereo Network for Depth Estimation. In *Proceedings of the AAAI Conference on Artificial Intelligence*, volume 37, 2348–2356.
- Wang, P.; Liu, L.; Liu, Y.; Theobalt, C.; Komura, T.; and Wang, W. 2021. NeuS: Learning Neural Implicit Surfaces by Volume Rendering for Multi-view Reconstruction. *Advances in Neural Information Processing Systems*, 34: 27171–27183.
- Wang, Y.; Skorokhodov, I.; and Wonka, P. 2022. Hf-neus: Improved surface reconstruction using high-frequency details. *Advances in Neural Information Processing Systems*, 35: 1966–1978.



- Wang, Y.; Skorokhodov, I.; and Wonka, P. 2023. PET-NeuS: Positional Encoding Tri-Planes for Neural Surfaces. In *Proceedings of the IEEE/CVF Conference on Computer Vision and Pattern Recognition*, 12598–12607.
- Wang, Y.; Zeng, Z.; Guan, T.; Yang, W.; Chen, Z.; Liu, W.; Xu, L.; and Luo, Y. 2023. Adaptive Patch Deformation for Textureless-Resilient Multi-View Stereo. In *Proceedings of the IEEE/CVF Conference on Computer Vision and Pattern Recognition*, 1621–1630.
- Wu, T.; Wang, J.; Pan, X.; Xu, X.; Theobalt, C.; Liu, Z.; and Lin, D. 2023. Voxurf: Voxel-based Efficient and Accurate Neural Surface Reconstruction. In *International Conference on Learning Representations (ICLR)*.
- Xu, Q.; Kong, W.; Tao, W.; and Pollefeys, M. 2022a. Multi-scale geometric consistency guided and planar prior assisted multi-view stereo. *IEEE Transactions on Pattern Analysis and Machine Intelligence*, 45(4): 4945–4963.
- Xu, Q.; Xu, Z.; Philip, J.; Bi, S.; Shu, Z.; Sunkavalli, K.; and Neumann, U. 2022b. Point-nerf: Point-based neural radiance fields. In *Proceedings of the IEEE/CVF Conference on Computer Vision and Pattern Recognition*, 5438–5448.
- Yang, B.; Bao, C.; Zeng, J.; Bao, H.; Zhang, Y.; Cui, Z.; and Zhang, G. 2022. Neumesh: Learning disentangled neural mesh-based implicit field for geometry and texture editing. In *European Conference on Computer Vision*, 597–614. Springer.
- Yao, Y.; Luo, Z.; Li, S.; Fang, T.; and Quan, L. 2018. Mvsnet: Depth inference for unstructured multi-view stereo. In *Proceedings of the European conference on computer vision (ECCV)*, 767–783.
- Yao, Y.; Luo, Z.; Li, S.; Zhang, J.; Ren, Y.; Zhou, L.; Fang, T.; and Quan, L. 2020. Blendedmvs: A large-scale dataset for generalized multi-view stereo networks. In *Proceedings of the IEEE/CVF conference on computer vision and pattern recognition*, 1790–1799.
- Yariv, L.; Gu, J.; Kasten, Y.; and Lipman, Y. 2021. Volume rendering of neural implicit surfaces. *Advances in Neural Information Processing Systems*, 34: 4805–4815.
- Yariv, L.; Kasten, Y.; Moran, D.; Galun, M.; Atzmon, M.; Ronen, B.; and Lipman, Y. 2020. Multiview neural surface reconstruction by disentangling geometry and appearance. *Advances in Neural Information Processing Systems*, 33: 2492–2502.
- Yu, Z.; Peng, S.; Niemeyer, M.; Sattler, T.; and Geiger, A. 2022. Monosdf: Exploring monocular geometric cues for neural implicit surface reconstruction. *Advances in neural information processing systems*, 35: 25018–25032.
- Zhang, J.; Yao, Y.; Li, S.; Fang, T.; McKinnon, D.; Tsin, Y.; and Quan, L. 2022. Critical regularizations for neural surface reconstruction in the wild. In *Proceedings of the IEEE/CVF Conference on Computer Vision and Pattern Recognition*, 6270–6279.
- Zhang, J.; Yao, Y.; and Quan, L. 2021. Learning signed distance field for multi-view surface reconstruction. In *Proceedings of the IEEE/CVF International Conference on Computer Vision*, 6525–6534.
- Zhang, Y.; Hu, Z.; Wu, H.; Zhao, M.; Li, L.; Zou, Z.; and Fan, C. 2023a. Towards Unbiased Volume Rendering of Neural Implicit Surfaces With Geometry Priors. In *Proceedings of the IEEE/CVF Conference on Computer Vision and Pattern Recognition*, 4359–4368.
- Zhang, Z.; Peng, R.; Hu, Y.; and Wang, R. 2023b. GeoMVS-Net: Learning Multi-View Stereo With Geometry Perception. In *Proceedings of the IEEE/CVF Conference on Computer Vision and Pattern Recognition*, 21508–21518.
- Zhu, B.; Yang, Y.; Wang, X.; Zheng, Y.; and Guibas, L. 2023. Vdn-nerf: Resolving shape-radiance ambiguity via view-dependence normalization. In *Proceedings of the IEEE/CVF Conference on Computer Vision and Pattern Recognition*, 35–45.